remote sensing

MDPI

Letter

An Investigation of a Novel Cross-Calibration Method of FY-3C/VIRR against NPP/VIIRS in the Dunhuang Test Site

Caixia Gao *,†, Yongguang Zhao *,†, Chuanrong Li, Lingling Ma, Ning Wang, Yonggang Qian and Lu Ren

Received: 30 November 2015; Accepted: 14 January 2016; Published: 21 January 2016
Academic Editors: Changyong Cao, Richard Müller and Prasad S. Thenkabail

Key Laboratory of Quantitative Remote Sensing Information Technology, Academy of Opto-Electronics, Chinese Academy of Sciences, Beijing 100094, China; crli@aoe.ac.cn (C.L.); llma@aoe.ac.cn (L.M.); wangning@aoe.ac.cn (N.W.); qianyg@aoe.ac.cn (Y.Q.); renlu@aoe.ac.cn (L.R.)
* Correspondence: caixiagao2010@hotmail.com (C.G.); zyggg22@163.com (Y.Z.); Tel.: +86-10-8217-8645 (C.G.)
† These authors contributed equally to this work.

Abstract: Radiometric cross-calibration of Earth observation sensors is an effective approach to evaluate instrument calibration performance, identify and diagnose calibration anomalies, and quantify the consistency of measurements from different sensors. In this study a novel cross-calibration method is proposed, taking into account the spectral and viewing angle differences adequately; the method is applied to the FY-3C/Visible Infrared Radiometer (VIRR), taking the Suomi National Polar-Orbiting Partnership (NPP)/Visible Infrared Imaging Radiometer Suite (VIIRS) as a reference. The results show that the relative difference between the two sets increases from January to May 2014, and becomes lower for the data on 24 July, 11 September, and 16 September, within approximately 10%. This phenomenon is caused by the updating of the calibration coefficients in the VIRR datasets with results from a vicarious method on June 2014. After performing an approximate estimation of the uncertainty, it is demonstrated that this calibration has a total uncertainty of 5.5%–6.0%, which is mainly from the uncertainty of the Bidirectional Reflectance Distribution Function model.

Keywords: cross-calibration; spectral adjustment; bidirectional reflectance distribution function model; FY-3C/VIRR; NPP/VIIRS

1. Introduction

To make full use of the ever-increasing EO satellite systems, radiometric calibration, especially post-launch calibration, is of critical importance for the various imaging sensor systems, because the performance of sensors is subject to change during launch and the subsequent exposure to the space environment [1–3]. On-board calibrators, reference to lamp sources and/or solar illumination or lunar illumination, and approaches using Earth scenes imaged in-flight are effective for operational calibration and monitoring of the performance of sensors. However, due to power, weight, and space restrictions, some satellites are not well characterized by on-board calibrators, especially in the solar reflective spectral region [4]; thus, the calibration approach using Earth scenes is significant.

Earth surfaces with suitable characteristics have long been used as benchmark or test sites to verify the post-launch radiometric calibration performance of satellite sensors. The associated methodologies are often referred to as vicarious calibration or cross-calibration [5]. Although vicarious calibration has been shown to be successful, its accuracy depends on the coincident surface measurements of test site, climate, and weather conditions, and this calibration technique is very complex, laborious, and

expensive. The cross-calibration approach uses terrestrial targets to transfer radiometric calibration between satellite sensors without coincident surface measurements; it has been explored for evaluating instrument calibration performance, identifying and diagnosing calibration anomalies [5]. Therefore, a number of national and international efforts have been made [6] on cross-calibration. Notable among them is the Global Space-based Inter-Calibration System (GSICS) initiated in 2005 by the World Meteorological Organization (WMO) and the Coordination Group for Meteorological Satellites (CGMS). GSICS aims to produce consistent and well-calibrated measurements from a variety of the international operational meteorological satellites, such as the serial satellites of Geostationary Operational Environmental Satellite system (GOES), Meteosat, FY, *etc.* [7].

The Visible Infrared Radiometer (VIRR) is one of the key instruments onboard the Chinese meteorological sun-synchronous satellite FY-3C, which was successfully launched on September 2013. Similar to the Advanced Very High Resolution Radiometer (AVHRR) and Multi-channel Visible and Infrared Scanning (MVIRS), VIRR has no on-board calibration system for the solar reflective channels, and its post-launch calibration depends on cross-calibration and vicarious calibration. However, because the vicarious calibration is performed once a year due to the cost and measurement conditions, cross-calibration becomes a valuable approach to characterize the performance of VIRR. Xu *et al.* have performed cross-calibration using the Moderate Resolution Imaging Spectroradiometer (MODIS) with the simultaneous nadir overpass (SNO) method [8]. However, the SNO method requires simultaneous nadir observation of the two sensors over the same target and has strict thresholds on the solar zenith and view angles. These requirements would result in less eligible image pairs, thereby reducing the frequency of cross-calibration. Therefore, this study preliminarily proposes a novel method for the cross-calibration between the sensors without strict viewing angle and spectral consistency, such that the sensors' performance could be monitored more frequently. This method is applied to the VIRR data in the solar reflective band with different viewing angles, referring to the well-calibrated Visible Infrared Imaging Radiometer Suite (VIIRS) onboard the Suomi National Polar-Orbiting Partnership (Suomi-NPP) spacecraft. The calibration accuracy of VIIRS is approximately 2% in most solar reflective bands [9].

Section 2 gives a detailed description of the methodology, including data description and the calibration approach. Section 3 shows the cross-calibration results of VIIRS and VIRR. Section 4 gives the uncertainty analysis, and some discussions are presented in Section 5. Conclusions are drawn in Section 6.

2. Methodology

2.1. Dataset Description

The Dunhuang test site is in the Gobi desert, approximately 35 km west of the city of Dunhuang. The test site was an operational radiometric calibration and validation site for Chinese satellite sensors in 2001, located on the eastern edge of the Kumutage Penniform Desert in Gansu province, Southwest China. The whole target area for vicarious calibration is situated on a stabilized alluvial fan, 30 km $\times$ 30 km in size [10]. The atmosphere is dry, clean, and typically has low levels of aerosol loading, making it beneficial for the calibration experiments; the site was chosen as one of the Committee on Earth Observation Satellites (CEOS) calibration and validation test sites.

The VIRR onboard FY-3C is a heritage instrument from the Multispectral Visible Infrared Scanning Radiometer (MVISR) onboard FY-1C and D. It provides images in 10 spectral bands between 0.44 and 12.5 μm, with a spatial resolution of 1.1 km at nadir, and it includes five visible-near infrared bands, two shortwave bands, and three middle and thermal infrared bands; its data records could be used for vegetation and ocean colour monitoring. VIIRS collects radiometric and imagery data in 22 spectral bands within the visible and infrared region ranging from 0.4 to 12.5 μm, including 16 moderate-resolution (750-m pixels) and five imagery resolution (375-m pixels) bands, plus one panchromatic "Day-Night Band". The VIIRS spectral data are calibrated and geolocated in ground

processing to generate Sensor Data Records (SDRs) [11,12]. The solar reflective bands of VIIRS, covering similar wavelength range as MODIS, are also calibrated by the solar diffuser (SD) and lunar observations, with a calibration accuracy of approximately 2% in most bands. Thus, bands M3, M4, I1, and I2 are used to cross-calibrate the corresponding VIRR bands 8, 9, 1, and 2; the characteristics of VIRR and VIIRS visible-near infrared channels are shown in Table 1 and Figure 1.

In addition, because the two sensors onboard different platforms have different overpassing times, only clear-sky scenes observed by both sensors are employed during 2014, so that the atmospheric effect resulting from different acquisition time could be reduced as much as possible, and no temporal matching is considered. In this study, a total of 11 scenes of VIRR images over Dunhuang site are acquired and used as the data source for cross-calibration with the corresponding VIIRS calibrated and geolocated SDR data. The dates and viewing geometries of these scenes are shown in Table 2. Note that some of the pairs have large differences in viewing direction between the two sensors, and this difference could incur larger calibration errors without an accurate Bi-directional Reflectance Distribution Function (BRDF) correction. As an example, Figure 2 shows the image of VIIRS band I2 (see Figure 2a) and VIRR band 2 (see Figure 2b) over the Dunhuang test site on 16 September 2014.

Table 1. The characteristics of VIRR and VIIRS visible-near infrared channels.

	Band	Centre Wavelength (μm)	Spectral Range (μm)	Spatial Resolution at Nadir (m)
FY-3C/VIRR	1	0.630	0.58–0.68	1100
	2	0.865	0.84–0.89	1100
	8	0.505	0.48–0.53	1100
	9	0.555	0.53–0.58	1100
NPP/VIIRS	I1	0.640	0.60–0.68	375
	I2	0.865	0.85–0.88	375
	M3	0.488	0.478–0.498	750
	M4	0.555	0.545–0.565	750

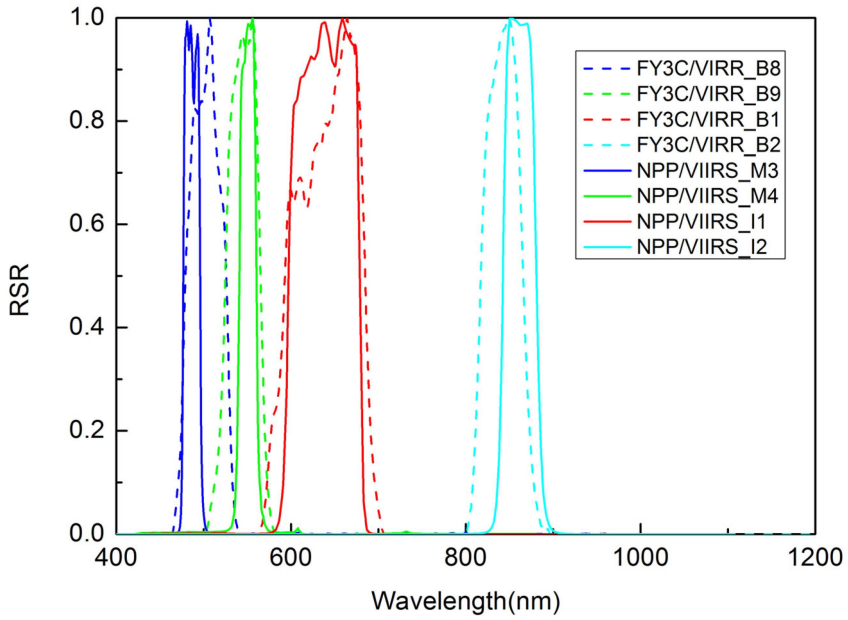

Figure 1. Spectral response functions of VIIRS and VIRR.

Table 2. The dates and viewing geometries of VIIRS and VIRR scenes.

Date	VIIRS				VIRR			
	SZA	**SAA**	**VZA**	**VAA**	**SZA**	**SAA**	**VZA**	**VAA**
8 January 2014	62.68	−173.55	37.31	74.33	64.50	162.11	21.07	−77.11
13 January 2014	62.03	−172.32	29.87	75.32	63.48	163.14	30.24	−75.71
24 January 2014	59.56	−174.62	37.35	74.32	61.78	160.39	23.50	−76.73
29 January 2014	58.40	−173.02	29.88	75.31	60.19	161.54	32.36	−75.38
13 March 2014	43.43	−171.67	37.61	74.22	45.60	157.12	29.94	−75.79
14 March 2014	42.73	−178.36	54.18	71.07	46.77	150.94	2.28	−87.08
24 March 2014	39.05	−171.91	43.72	73.23	41.62	154.53	22.92	−76.86
6 May 2014	24.28	−165.10	48.87	72.26	26.86	147.57	18.94	−77.53
24 July 2014	21.72	−156.56	29.69	75.37	22.27	152.56	47.02	−72.89
11 September 2014	36.16	−168.11	49.32	72.22	37.19	159.92	30.21	−75.77
16 September 2014	38.40	−165.41	43.84	73.27	38.56	163.97	37.89	−74.55

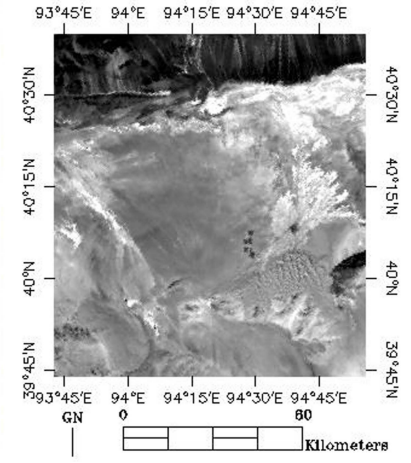

(**a**)

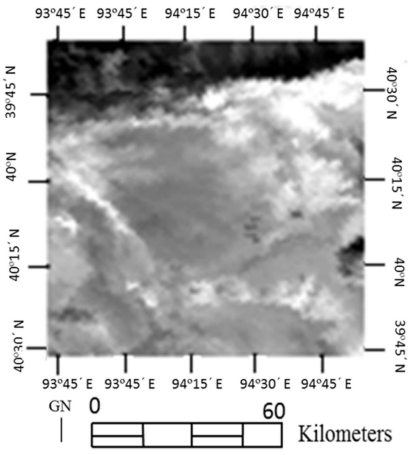

(**b**)

Figure 2. The images of VIIRS band I2 (**a**) and VIRR band 2 (**b**) over the Dunhuang test site on 16 September 2014.

2.2. Cross-Calibration Approach

The cross-calibration method involves comparison of the radiance/reflectance measured by the calibrated sensor with that measured by a well-calibrated sensor as a reference. This exercise can be

reduced to spatiotemporal coincidences, *i.e.*, acquisition by both sensors at the same time and with the same viewing geometries (for example, the SNO method). Nevertheless, such coincidences are not very frequent when comparing two sensors with different orbits, altitudes, cycles, and local equatorial crossing time. In these conditions, the reference is, in general, not acquired at the same time for exactly the same spectral range and for the same viewing geometry [13]. For this reason, some corrections must be applied to take into account these aspects.

To alleviate the impact of viewing geometry on the cross-calibration, the Bidirectional Reflectance Distribution Function (BRDF) characteristics of Dunhuang site measured in 2011 with SVC HR1024 spectrometer are used. Measurements were acquired with the viewing zenith angle scanning from 0° to 70° with a step of 14°, and the relative azimuth angles between the sun and viewing direction varied from 0° to 180°, with a step of 30°. Seven datasets of hemispherical scanning measurements were used with the solar zenith angle ranging from 29° to 52°. Examples of the multi-angle Bidirectional Reflectance Factor (BRF) measurements corresponding to VIIRS bands M3, M4, I1, and I2 are shown in Figure 3. The figure shows a general increasing trend towards the backward scattering direction for these bands. In this study, first, with the atmospheric parameters at the VIIRS scenes' acquisition time [the water vapor content (WVC) extracted from the National Centers for Environmental Prediction (NCEP) reanalysis data, the ozone content extracted from the product of Ozone Monitoring Instrument (OMI) onboard the Aura satellite, and the assumed visibility of 40 km (see Table 3), the surface reflectance of Dunhuang site is derived from VIIRS reflectance at the top of atmosphere (TOA) using the radiative transfer model 6S. Next, the angular effect of surface reflectance is corrected with the BRDF model proposed by Roujean *et al.* [14], fitted with the multi-angle BRF measurements, and the surface reflectance along with VIRR viewing direction could be acquired. Subsequently, based on the atmospheric parameters at the VIRR scene acquisition times, the corresponding TOA reflectance is simulated using the 6S model. In this study, the default solar model in the 6S radiative transfer model is used to characterize the solar irradiance [15].

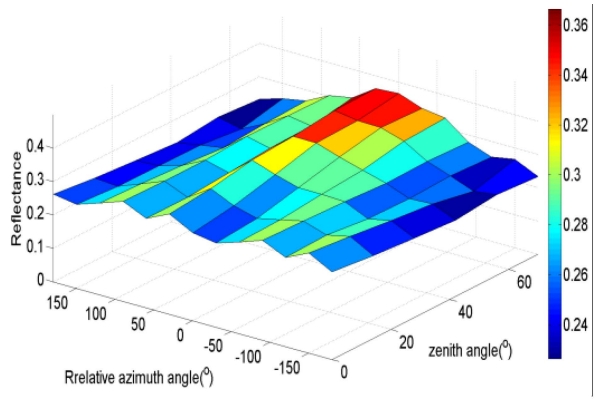

(**a**)

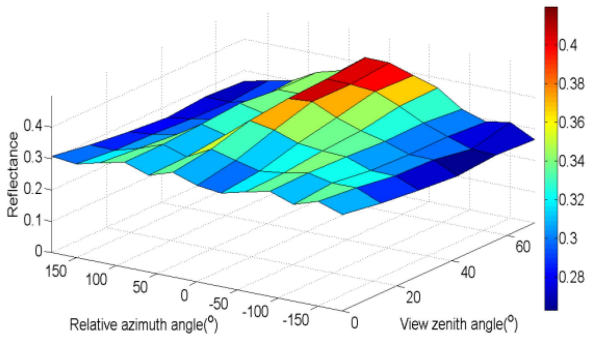

(**b**)

Figure 3. *Cont.*

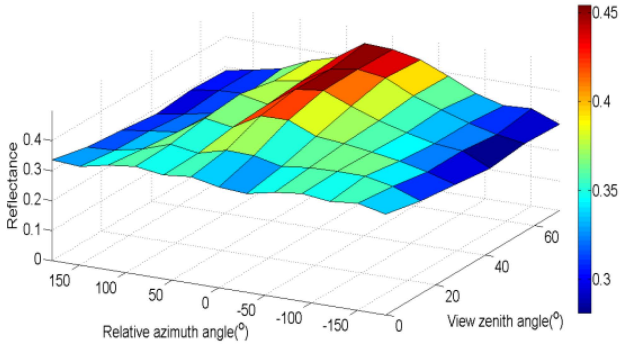

(**c**)

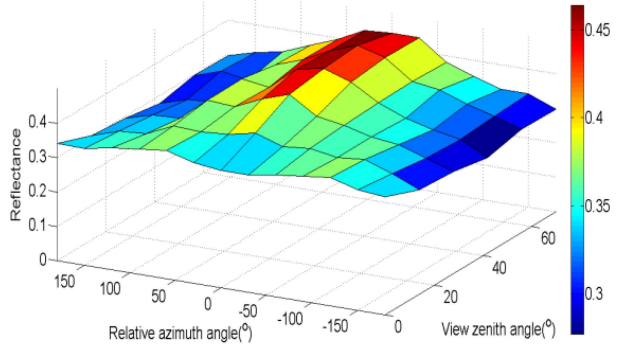

(**d**)

Figure 3. Measured Bidirectional Reflectance Factor of the Dunhuang site. (**a**) VIIRS M3; (**b**) VIIRS M4; (**c**) VIIRS I1; and (**d**) VIIRS I2.

Table 3. Atmosphere parameters at VIIRS and VIRR acquisition times.

Date	WVC at VIIRS Scenes Acquisition Time ($g \cdot cm^{-2}$)	WVC at VIRR Scenes Acquisition Time ($g \cdot cm^{-2}$)	Ozone (atm-cm)	Visibility (km)
8 January 2014	0.260	0.231	0.334	
13 January 2014	0.269	0.171	0.335	
24 January 2014	0.369	0.464	0.332	
29 January 2014	0.461	0.526	0.327	
13 March 2014	0.298	0.272	0.341	
14 March 2014	0.635	0.619	0.341	40.0
24 March 2014	0.551	0.524	0.347	
6 May 2014	0.751	0.754	0.280	
24 July 2014	1.234	1.198	0.280	
11 September 2014	0.848	0.844	0.297	
16 September 2014	0.397	0.318	0.297	

Different applications and technological developments in Earth observation necessarily require different spectral coverage [16]. Thus, spectral bands differ significantly among sensors, even for bands designed to observe at the same region of the electromagnetic spectrum; as a result, these sensors yield fundamentally different measurements that are not directly comparable. To remove the effect of spectral characteristics on cross-calibration, the spectral band adjustment factor k in a given spectral band i is calculated as a ratio of the TOA reflectance from two sensors with a simulation method. In this method, a series of TOA reflectance for VIIRS and VIRR sensors in a given spectral bands i are calculated using the 6S model. The band surface reflectances, varying from 0.1 to 0.5 with a step of 0.1, are used as inputs to drive the 6S model, together with the selected atmospheric states, the

sensor's spectral response function, and the illumination and viewing geometries. Subsequently, the corresponding spectral band adjustment factor k_i is fitted by linear regression method.

After alleviating the impact of viewing geometry and spectral characteristics, the measured TOA reflectance of VIRR in a given band i could be evaluated with the simulated VIRR reflectance values. The flowchart is shown in Figure 4:

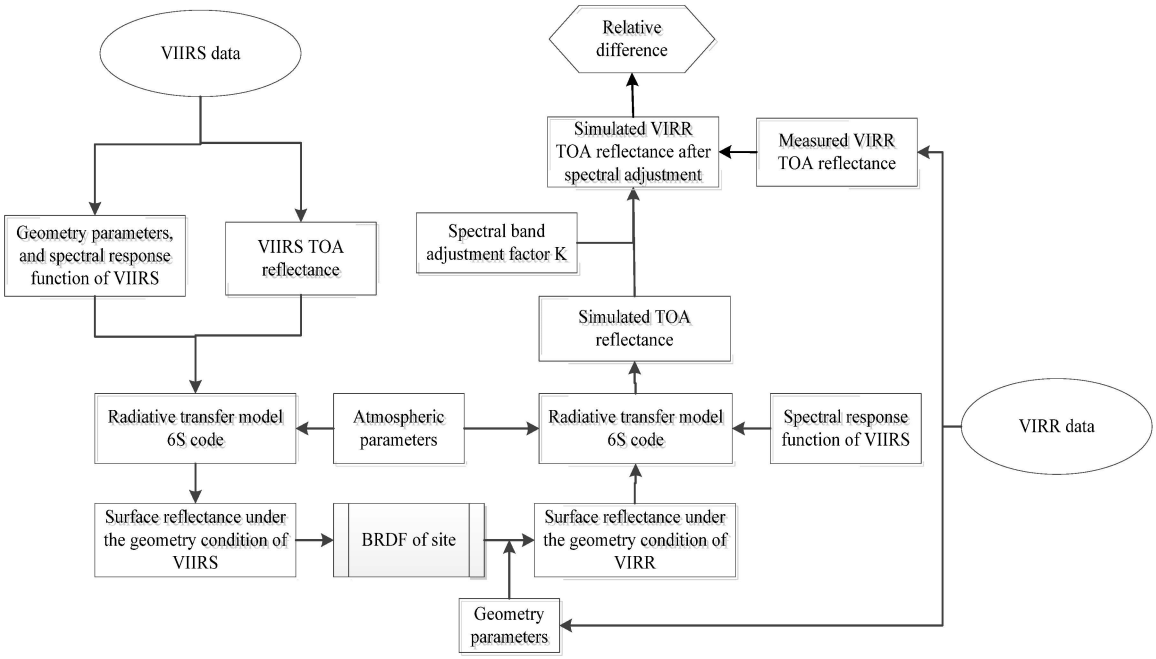

Figure 4. The flowchart of the cross-calibration procedure.

3. Results

To perform this cross-calibration, a common calibration area over the Dunhuang site is selected with geographic location of the top-left corner (40.25°N, 94.25°E) and the bottom-right corner (40.1°N, 94.5°E) of the area. This area has a coverage of approximately 2400 pixels and 1100 pixels in the VIIRS images at a spatial resolution of 350 m and 750 m, respectively, and 725 pixels in the VIRR images. Table 4 depicts its mean digital number (DN) values and standard deviation.

Table 4. Mean DN values and its standard deviation.

Date	Mean Value				STD Value			
	B8	B9	B1	B2	B8	B9	B1	B2
8 January 2014	140.95	145.17	83.62	87.08	1.92	2.51	1.89	2.57
13 January 2014	144.78	149.34	86.13	90.15	2.06	2.75	2.02	2.72
24 January 2014	153.59	160.44	92.99	95.53	2.25	2.95	2.21	2.87
29 January 2014	169.06	175.29	99.84	101.87	2.82	3.07	2.15	2.60
13 March 2014	215.26	232.47	136.25	145.70	3.59	4.68	3.40	4.66
14 March 2014	222.88	240.54	140.89	149.22	3.42	4.51	3.39	4.53
24 March 2014	230.96	251.25	147.83	156.00	3.25	4.14	3.08	4.06
6 May 2014	265.87	293.62	175.70	185.71	4.79	6.24	5.05	7.20
24 July 2014	249.63	269.75	156.51	155.94	3.72	4.65	3.50	4.88
11 September 2014	219.52	239.85	140.87	142.15	5.22	6.96	4.85	6.25
16 September 2014	218.79	237.21	139.20	144.28	4.36	5.65	4.00	5.35

With the aid of the atmospheric parameters (see Table 3), the atmospheric correction of VIIRS is performed for the aforementioned VIIRS datasets via 6S code, and then the derived surface reflectance

are corrected with the BRDF model. The scatterplot of the VIIRS TOA reflectance and the derived surface reflectance (see Figure 5), and the scatter plot of the derived surface reflectance and the BRDF corrected values under the geometry condition of VIRR (see Figure 6) are shown below. Note that the atmosphere effect on the VIIRS M3 band is higher than for the other three bands, and the differences in Figure 6 denote the sole influence of the BRDF correction with positive or negative values, which depend on differences between the viewing geometries of the two sensors. With the aforementioned method, the spectral band adjustment factor for each of the image pairs is calculated. Figure 7 shows the spectral band adjustment factor on 24 July 2014. With the aid of the spectral band adjustment factor, surface reflectance and corresponding atmospheric parameters, the simulated VIRR TOA reflectance is acquired via 6S (see Figure 8) and is compared with the measured ones (see Figure 9). Note that the relative difference between the two sets increases from January to May 2014, with a maximum of more than 45%, and the relative differences are lower for the data on 24 July, 11, 16 September, approximately within 10%. The lower relative differences would result from the fact that VIRR has been calibrated using the vicarious method on June 2014, and the calibration coefficients in the datasets were updated. In contrast, the pre-launch calibration coefficient was adopted for these datasets before June 2014. Table 5 shows a comparison between the pre-launch calibration coefficient (gain) of the VIRR sensor and the post-launch one on June, 2014. Note that a large variation is presented on the gain values of the VIRR sensor.

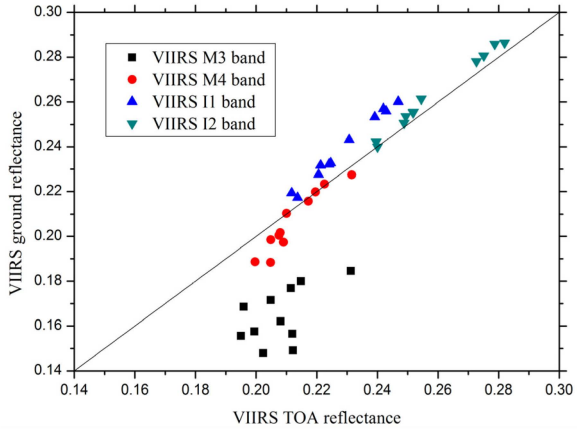

Figure 5. Scatterplot of the VIIRS TOA reflectance and its surface reflectance after atmospheric correction.

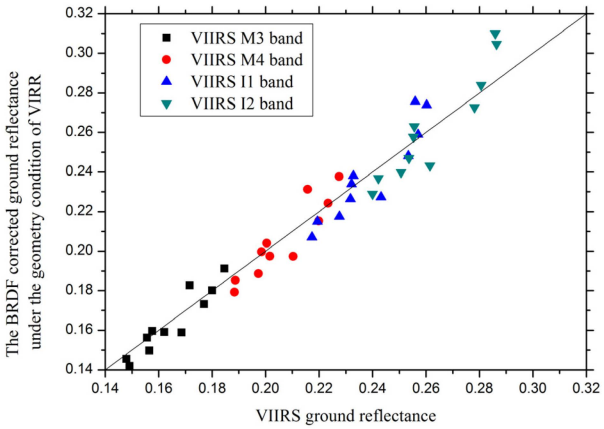

Figure 6. Scatterplot of the VIIRS surface reflectance and the BRDF corrected reflectance values under the geometry condition of VIRR.

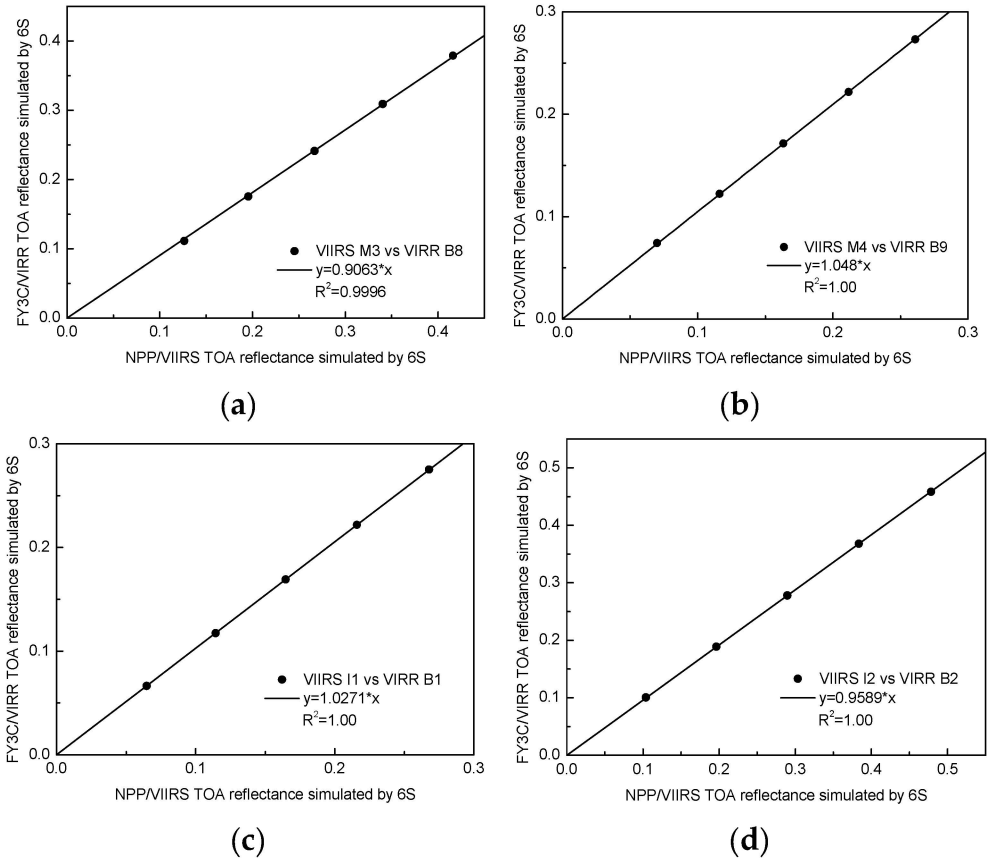

Figure 7. Spectral band adjustment factor between VIIRS and VIRR on 24 July 2014. (**a**) VIIRS M3 *vs.* VIRR B8; (**b**) VIIRS M4 *vs.* VIRR B9; (**c**) VIIRS I1 *vs.* VIRR B1; (**d**) VIIRS I2 *vs.* VIRR B2.

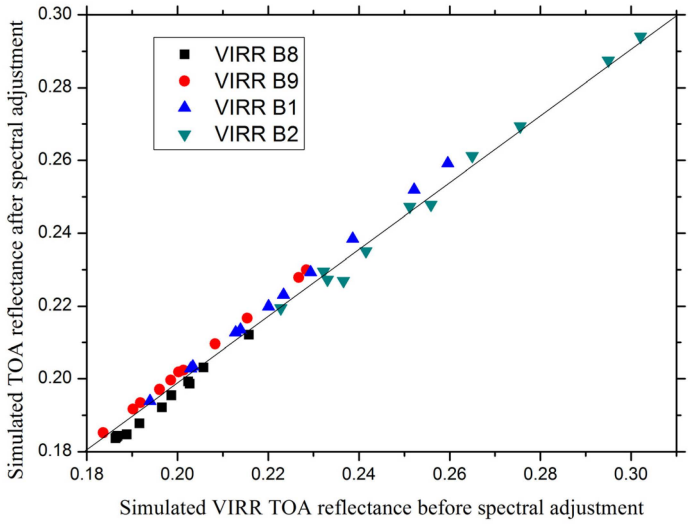

Figure 8. Scatterplot of the simulated VIRR TOA reflectance before spectral adjustment and the corresponding values after spectral adjustment.

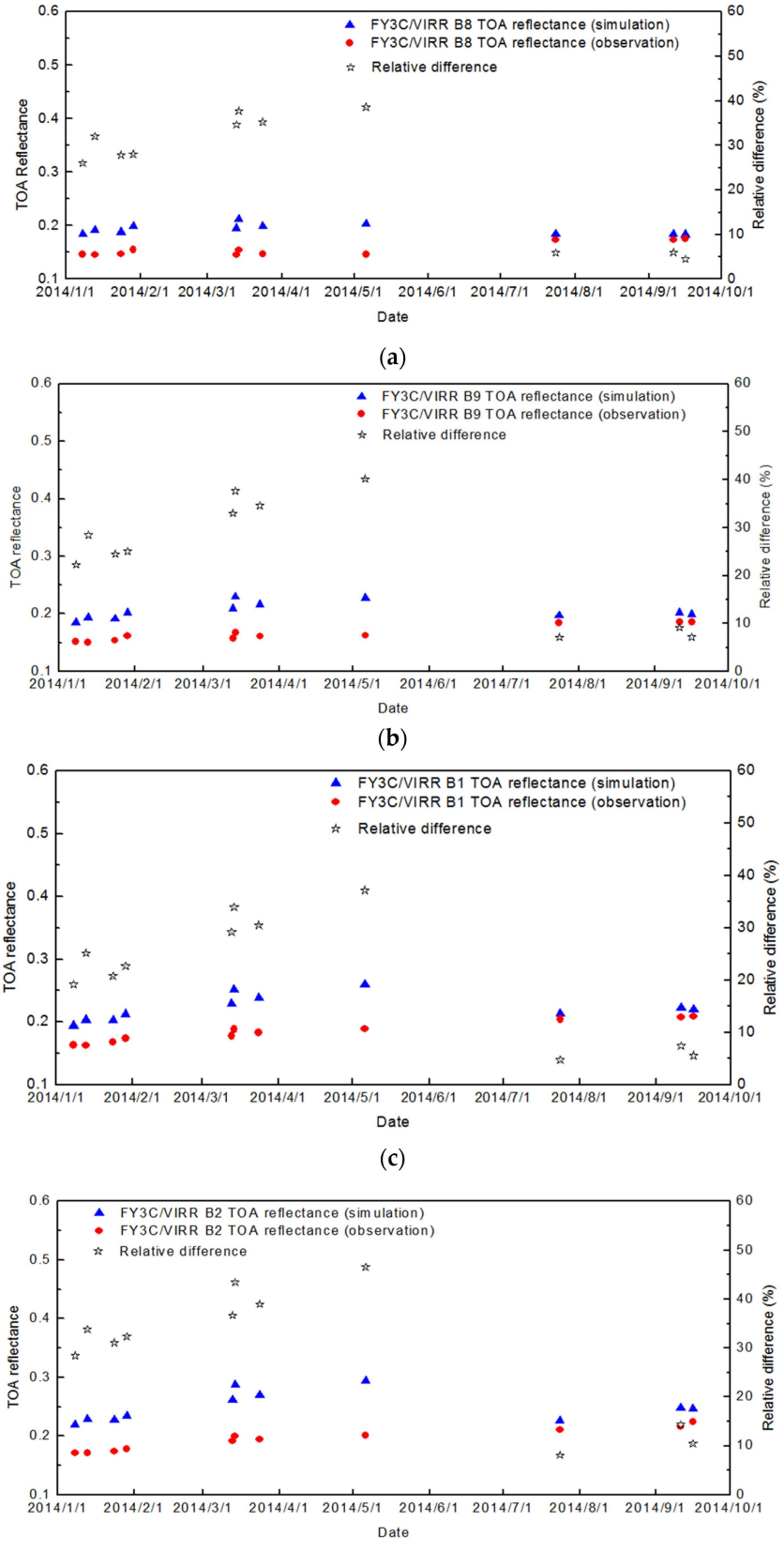

Figure 9. Scatterplot of the simulated VIRR TOA reflectance values after the spectral adjustment and the observed values. (**a**) VIRR B8; (**b**) VIRR B9; (**c**) VIRR B1; and (**d**) VIRR B2.

Table 5. The comparison between the pre-launch calibration coefficient (gain) of the VIRR sensor and the post-launch calibration coefficient (gain).

VIRR Band	Pre-Launch	Post-Launch (on June 2014)	Relative Difference
1	0.10118	0.12549	24.03%
2	0.10126	0.1297	28.09%
8	0.05061	0.06502	28.47%
9	0.05063	0.06455	27.49%

4. Uncertainty Analysis

Although the view geometry and spectral discrepancies between two sensors are reduced as much as possible in this study via BRDF correction and spectral adjustment, the accuracy of cross-calibration is still affected by several factors, such as the uncertainty of the BRDF model, atmosphere parameters, (WVC, visibility, ozone content, and aerosol model, *etc.*), image registration, 6S model, *etc.* Since not all the factors could be quantified, a rough estimation is performed in terms of the following factors in this study:

1. The uncertainty caused by the VIIRS calibration ($\sigma_{1,i}$ (band number i = 8, 9, 1, and 2)): the uncertainty of the VIIRS calibration is approximately 2% (see the second row in Table 6).
2. The uncertainty that is caused by the 6S model ($\sigma_{2,i}$ (band number i = 8, 9, 1, and 2)): according to the error transfer theory, the error of the 6S model (σ_{6s}), which is estimated to be approximately 2%, caused by this model error ($\sigma_{2,i} = \sqrt{2}\sigma_{6s}$) is approximately 2.83% (see the third row in Table 6).
3. The uncertainty caused by the BRDF effect ($\sigma_{3,i}$(band number i = 8, 9, 1, and 2)): the uncertainty of the fitted BRDF model proposed by Roujean is approximately 5%, resulting in an uncertainty within 4.5% of the simulated VIRR TOA radiance (see the fourth row in Table 6).
4. The uncertainty that is caused by the atmospheric parameters

    - In this study, the aerosol type is assumed as the continental aerosol model, which would create an error in the TOA reflectance simulation of VIRR because the Dunhuang test site has a mixed aerosol type of the continental and desert models. To analyze the effect of aerosol type on the cross-calibration ($\sigma_{4,i}$ (band number i = 8, 9, 1, and 2)), spectral adjustment factors and a new group of VIRR TOA reflectance for a given band i is generated when the desert aerosol model is used, and the relative differences are also computed (see the fifth row in Table 6). Similarly, the visibility is changed by $\pm$10 km to analyze the uncertainty caused by aerosol type ($\sigma_{5,i}$ (band number i = 8, 9, 1, and 2), see the sixth row in Table 6). The results demonstrate that the uncertainty resulting from the aerosol type and the visibility are all within 1%.
    - The WVC and ozone contents are also important parameters in this cross-calibration approach. To investigate their effects, similar to the analysis method of visibility, it could be found that the 20% uncertainty in WVC and 10% uncertainty in ozone content would cause an uncertainty within 0.5% ($\sigma_{6,i}$ (band number i = 8, 9, 1, and 2)) and 0.2% ($\sigma_{7,i}$ (band number i = 8, 9, 1, and 2)), respectively, to the cross-calibration (see the seventh and eighth rows in Table 6).

5. Image co-registration error ($\sigma_{8,i}$ (band number i = 8, 9, 1, and 2)): the relative location offset of the cross-calibration test site in two images is inevitable, thereby affecting the accuracy of the cross-calibration. In this study, a sliding window method is used [17] to estimate that the image co-registration error would cause an uncertainty of approximately 0.3%–0.5% (see the ninth row in Table 6).

From these analyses, the total uncertainty for spectral band i (σ_i, i = 8, 9, 1, and 2) in the cross-calibration could be estimated with $\sigma_i = \sqrt{\sum_{j=1}^{8} \sigma_{j,i}^2}$ (j is the index of uncertainty terms); note that the uncertainty in the calibration for the four spectral bands is 5.5%–6.0%.

Table 6. Uncertainty analysis results.

Source	FY/VIRR B8	FY/VIRR B9	FY/VIRR B1	FY/VIRR B2
VIIRS calibration accuracy	2.00%	2.00%	2.00%	2.00%
6S model	2.83%	2.83%	2.83%	2.83%
BRDF	4.13%	4.33%	4.56%	4.42%
Aerosol type	0.51%	0.95%	0.97%	1.07%
Visibility	0.65%	0.56%	0.50%	0.32%
WVC	0.01%	0.01%	0.02%	0.41%
Ozone content	0.16%	0.18%	0.16%	0.01%
Image co-registration	0.31%	0.36%	0.44%	0.57%
Total uncertainty	5.47%	5.67%	5.85%	5.77%

5. Discussion

With the development of remote sensing technology and the urgent need for its quantitative application, much more accurate and higher-frequency radiometric calibration is required to monitor sensor performance. FY-3C/VIRR was launched in 2013 without an onboard calibrator, so that its calibration mainly depends on the various calibrations and cross-calibration. Due to the limitation of SNO cross-calibration method on the solar zenith and view angles, a new cross-calibration method is proposed that has great application potential. In this method, to eliminate the spectral difference between two sensors, the spectral adjustment factor is calculated with a linear regression method for reducing its low sensitivity to the variation of surface reflectance. Furthermore, to account for their viewing geometries differences between two sensors, a BRDF model is constructed with the measured BRF over a uniform area of Dunhuang site. After these corrections, the simulated VIRR TOA reflectance is acquired and is inter-compared with the measured one. Compared to the SNO method, the cross-calibration method can be performed without strict thresholds on view angles, and thus the performance of VIRR could be monitored more frequently with VIIRS, MODIS, *etc*. In addition, the method also could be applied to other sensors. However, it can be found that the accuracy of this method strongly depends on the accuracy of BRDF model, so the image pairs with very large viewing geometries would induce much higher uncertainties on the calibration. Therefore, in the future, further studies on the BRDF model, more accurate BRDF measurements, and the validation of the method over different surface types and synchronized ground measurements are required.

6. Conclusions

In this study, NPP/VIIRS was used as a reference sensor to cross-calibrate the FY-3C/VIRR with a proposed method to monitor its radiometric performance, taking into account the discrepancies in the geometries and spectral coverage between the two sensors. The results preliminary demonstrate that there exists a large difference between VIRR and VIIRS; this might be partly caused by the degradation of VIRR. The relative difference between the two datasets increases from January to May 2014, and is lower for the data on 24 July, 11 September, and 16 September, approximately within 10%. The phenomenon is because the calibration coefficients in the VIRR datasets were updated in June 2014, with results from the vicarious method. Furthermore, through an approximate error analysis, it is found that the total uncertainty for the cross-calibration is 5.5%–6.0%. Among the various factors, the uncertainties of atmosphere parameters have little effect on the accuracy of the cross-calibration; the accuracy of BRDF was found to be the main source affecting the calibration accuracy. Thus, a more accurate BRDF model is required to promote this method in the future for long-term application.

Acknowledgments: The work has been supported by the National High Technology Research and Development Program of China 863 program (2013AA122102) and by the National Natural Science Foundation of China (41301387). The authors thank the China Centre for Resources Satellite Data and Application for providing BRF measurement over the Dunhuang site, and the China Meteorological Administration for providing FY-3C satellite data. Thanks are also given to the anonymous reviewers.

Author Contributions: Caixia Gao and Chuanrong Li conceived and designed the experiments; Yongguang Zhao performed the experiments; Lingling Ma and Ning Wang analysed the data; Yonggang Qian contributed to the data processing; Lu Ren download the satellite data; Caixia Gao wrote the paper.

Conflicts of Interest: The authors declare no conflict of interest.

References

1. Teillet, P.M.; Fedosejevs, G.; Thome, K.J.; Barker, J.L. Impacts of spectral band difference effects on radiometric cross-calibration between satellite sensors in the solar-reflective spectral domain. *Remote Sens. Environ.* **2007**, *110*, 393–409. [CrossRef]
2. Kuusk, A.; Kuusk, J.; Lang, M.; Lükk, T. Vicarious calibration of the PROBA/CHRIS imaging spectrometer. *Photogramm. J. Finl.* **2010**, *22*, 46–59.
3. Gao, C.X.; Jiang, X.G.; Li, X.B.; Li, X.H. The cross-calibration of CBERS-02B/CCD visible-near infrared channels with Terra/MODIS channels. *Int. J. Remote Sens.* **2013**, *34*, 3688–3698. [CrossRef]
4. Ham, S.H.; Sohn, B.J. Assessment of the calibration performance of satellite visible channels using cloud targets: Application to Meteosat-8/9 and MTSAT-1R. *Atmos. Chem. Phys.* **2010**, *10*, 11131–11149. [CrossRef]
5. Teillet, P.M.; Barsi, J.A.; Chander, G.; Thome, K.J. Prime candidate earth targets for the post-launch radiometric calibration of space-based optical imaging instruments, optical engineering applications. *Int. Soc. Opt. Photonics* **2007**. [CrossRef]
6. Chander, G.; Hewison, T.J.; Fox, N.; Wu, X.; Xiong, X.; Blackwell, W.J. Overview of intercalibration of satellite instruments. *IEEE Trans. Geosci. Remote Sens.* **2013**, *51*, 1056–1080. [CrossRef]
7. Yu, F.F.; Wu, X.Q.; Goldberg, M. Recent operational status of GSICS GEO-LEO and GEO-GEO inter-calibrations at NOAA/NESDIS. In Proceedings of the IEEE International Geoscience and Remote Sensing Symposium, Vancouver, BC, Canada, 24–29 July 2011; pp. 989–992.
8. Xu, N.; Chen, L.; Wu, R.H.; Hu, X.Q.; Sun, L.; Zhang, P. In-flight intercalibration of FY-3C visible channels with AQUA MODIS. *Proc. SPIE* **2014**. [CrossRef]
9. VIIRS SDR Science Team. Visible Infrared Imaging Radiometer Suite (VIIRS) Sensor Data Record (SDR) Error Budget, 19 December 2013. Available online: http://www.star.nesdis.noaa.gov/smcd/spb/nsun/snpp/VIIRS/VIIRS_SDR_Error_Budget-2013.pdf (accessed on 16 October 2015).
10. USGS. Remote Sensing Technologies. Available online: http://calval.cr.usgs.gov/rst-resources/sites_catalog/radiometric-sites/dunhuang (accessed on 7 October 2015).
11. Cao, C.; Shao, X.; Uprety, S. Detecting light outages after severe storms using the S-NPP/VIIRS day/night band radiances. *IEEE Trans. Geosci. Remote Sens. Lett.* **2013**, *10*, 1582–1586. [CrossRef]
12. Cao, C.; de Luccia, F.J.; Xiong, X.X.; Wolfe, R.; Weng, F. Early on-orbit performance of the visible infrared imaging radiometer suite onboard the suomi national polar-orbiting Partnership (S-NPP) satellite. *IEEE Trans. Geosci. Remote Sens.* **2014**, *52*, 1142–1156. [CrossRef]
13. Lacherade, S.; Fougnie, B.; Henry, P.; Gamet, P. Cross calibration over desert sites: Description, methodology, and operational implementation. *IEEE Trans. Geosci. Remote Sens.* **2013**, *51*, 1098–1113. [CrossRef]
14. Roujean, J.L.; Leroy, M.; Deschamps, P.Y. A bi-directional reflectance model of the Earth's surface for the correction of remote sensing data. *J. Geophys. Res.* **1992**, *97*, 20455–20468. [CrossRef]
15. Neckel, H.; Labs, D. The solar radiation between 3300 and 12500. *Sol. Phys.* **1984**, *90*, 205–258. [CrossRef]
16. Chander, G.; Mishra, N.; Helder, D.L.; Aaron, D.; Choi, T.; Angal, A.; Xiong, X. Use of EO-1 Hyperion data to calculate spectral band adjustment factors (SBAF) between the L7 ETM+ and Terra MODIS sensors. In Proceedings of the IEEE International Geoscience and Remote Sensing Symposium (IGARSS), Honolulu, HI, USA, 25–30 July 2010; pp. 1667–1670.
17. Wang, Z.; Xiao, P.F.; Gu, X.F.; Feng, X.Z.; Li, X.Y.; Gao, H.L.; Li, H.; Lin, J.T.; Zhang, X.L. Uncertainty analysis of cross-calibration for HJ-1 CCD camera. *Sci. China* **2013**, *56*, 713–723. [CrossRef]